A potentially implantable glucose fuel cell with Raney-platinum film electrodes for improved hydrolytic and oxidative stability

S. Kerzenmacher [a,*], U. Kräling [a], T. Metz [a], R. Zengerle [a,b], F. von Stetten [a]

[a] Laboratory for MEMS Applications, Department of Microsystems Engineering – IMTEK, University of Freiburg, Georges-Koehler-Allee 103, D-79110 Freiburg, Germany
[b] Centre for Biological Signalling Studies (bioss), Albert-Ludwigs-Universität Freiburg, Germany
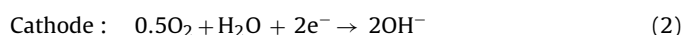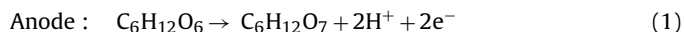
ABSTRACT

We present an improved abiotically catalyzed glucose fuel cell, intended as energy harvesting tissue implantable power supply for medical implants. The fuel cell is constructed from a Raney-platinum film cathode deposited on a silicon substrate with micro-machined feedholes for glucose permeability, arranged in front of a Raney-platinum film anode. A novelty is the application of platinum for both electrodes and the complete abdication of hydrogel binders. This overcomes the limited stability against hydrolytic and oxidative attack encountered with previous glucose fuel cells fabricated from activated carbon particles dispersed in a hydrogel matrix. During performance characterization in phosphate buffered saline under physiological concentrations of glucose and oxygen the diffusion resistance to be expected from tissue capsule formation was taken into account. Despite the resulting limited oxygen supply, the Raney-platinum fuel cells exhibit a power density of up to $(4.4 \pm 0.2)\,\mu W\,cm^{-2}$ at 7.0% oxygen saturation. This exceeds the performance of our previous carbon-based prototypes, and can be attributed to the higher catalytic activity of platinum cathodes and in particular the increased oxygen tolerance of the Raney-platinum film anodes.

© 2010 Elsevier B.V. All rights reserved.

1. Introduction

1.1. A sustainable fuel cell power supply for medical implants

Implantable glucose fuel cells employing abiotic catalyst (e.g. noble metals, activated carbon) are a newly rediscovered approach to realize a battery-independent power supply for medical implants [1]. With this concept electricity is directly generated from glucose and oxygen available in body fluids. As main reaction product of glucose oxidation on platinum electrodes gluconic acid has been identified [2]. The predominant electrode reactions are thus given as [3]:

$$\text{Anode}: \quad C_6H_{12}O_6 \rightarrow C_6H_{12}O_7 + 2H^+ + 2e^- \tag{1}$$

$$\text{Cathode}: \quad 0.5O_2 + H_2O + 2e^- \rightarrow 2OH^- \tag{2}$$

In a favorable embodiment of such a fuel cell a glucose-permeable cathode, fabricated from hydrogel-dispersed activated carbon, is situated in front of the anode [3]. The prime advantage of this concept is that reactant access to the fuel cell from one side is sufficient, enabling its integration directly onto the surface of medical implants [4] at minimized geometric footprint.

A drawback of previous glucose-permeable electrodes (cathodes) has been their limited stability against hydrolytic and oxidative attack, as they were fabricated from catalyst particles embedded in a poly(vinyl alcohol)–poly(acrylic acid) hydrogel matrix [5,6] (Fig. 1a). Furthermore, the low electrical conductivity of hydrogel-catalyst compounds mandates the use of mesh-like current collectors embedded within the electrodes, leading to relatively thick structures in the range of several hundred μm [3,6].

1.2. Raney-platinum film electrodes

A chemically resistant alternative to hydrogel-bound electrodes are Raney-platinum film electrodes, originally fabricated by extraction of the non-noble components from thin foils of platinum–nickel and platinum/tungsten–nickel alloys [7]. Since the biocompatibility of nickel is questionable, we recently presented an alternative fabrication route employing zinc as less problematic alloying partner [8] (reference to be updated by publisher). Furthermore, we demonstrated that a similar fabrication concept using aluminum as alloying partner is also suitable to fabricate sub-μm thin platinum cathodes for oxygen reduction,

---

* Corresponding author. Tel.: +49 761 2037328; fax: +49 761 2037322.
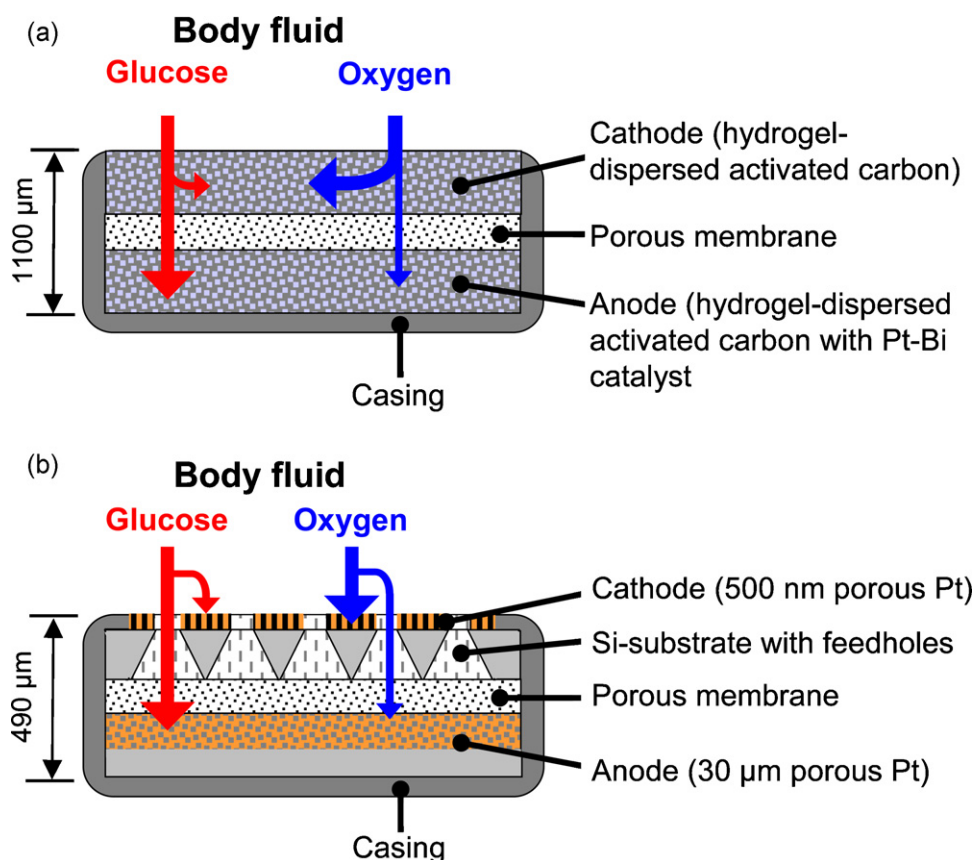*E-mail address:* kerzenma@imtek.de (S. Kerzenmacher).

Fig. 1. Comparison of two construction concepts for abiotically catalyzed glucose fuel cells. (a) State-of-the-art approach with hydrogel-dispersed activated carbon electrodes [6]. (b) Binder-less concept presented in this work, employing a thin-layer platinum cathode deposited on a silicon substrate with micro-machined feedholes, and a self-supporting platinum anode.

supported on a silicon substrate [9] (reference to be updated by publisher). These cathodes show higher catalytic activity than activated carbon, and exhibit sufficient tolerance towards glucose to be efficiently used in an implantable glucose fuel cell. However, prerequisite for the application of the novel Raney-platinum cathodes in a fuel cell with stacked electrode arrangement is that the exterior cathode allows for glucose diffusion to the interior anode.

We thus propose the micro-fabrication of well-defined feedholes into the silicon substrate supporting the Raney-platinum cathode (Fig. 1b). The present work reports on the dimensioning of feedhole size towards sufficient reactant supply at the electrodes by means of diffusion simulation, and the characterization of correspondingly fabricated fuel cells in terms of electrode polarization and overall power density under physiological concentrations of glucose and oxygen. In both, simulation and experimental characterization the additional diffusion resistance expected from tissue capsule formation [10] around the fuel cell upon implantation in body tissue is taken into account.

2. Feedhole dimensioning

A central aspect of the proposed glucose fuel cell is the size of feedholes in the silicon substrate supporting the Raney-platinum cathodes. On the one hand these feedholes need to be sufficiently large to sustain the required diffusive glucose flux to the anode. On the other hand, increasing feedhole size reduces the geometrical area available for cathode deposition, resulting in increased local current density and thus more pronounced electrode polarization.

In terms of reactant supply the fabrication of tapered feedholes by anisotropic KOH-etching of ⟨1 0 0⟩-oriented silicon wafers [11,12] is advantageous. Compared to straight feedholes of the same width at the cathode side (and thus geometrical area available for cathode deposition) the opening angle of the tapered feedholes (Fig. 2) promises lower diffusion resistance as well as more homogenous glucose distribution at the anode. While the modeling of the electrochemical behavior of the electrodes is beyond the scope of this work, the application of numerical simulation for dimensioning of the tapered feedholes towards sufficient reactant supply to the fuel cell electrodes is described in the following.

2.1. Diffusion model

Diffusive reactant flux in the fuel cell was modeled using the *CFD-ACE+ 2006* computational fluid dynamics software package (ESI Group, Paris, France). Thereto, the glucose fuel cell was reduced to a three-dimensional unit cell formed around a single feedhole (Fig. 2). Coming from the body tissue, the configuration of the model region is as follows: as diffusion barrier (R1) accounting for tissue capsule formation a 136-μm thick porous membrane (Supor-450, 0.45 μm pore size, Pall, East Hills, New York, USA) is placed in front of the cathode. Its diffusion resistance is comparable to typical capsules forming around implanted devices [9,10]. The cathode itself is situated on top of the 300-μm thick silicon support with the micro-machined tapered feedhole (R2). Between cathode support and anode a second 136-μm thick porous membrane is placed for electrical insulation (R3). Configuration and dimensions of the unit cell are illustrated in Fig. 2. For numerical analysis, the feedhole length l_f was kept constant at 1818 μm while its width w_f was var-
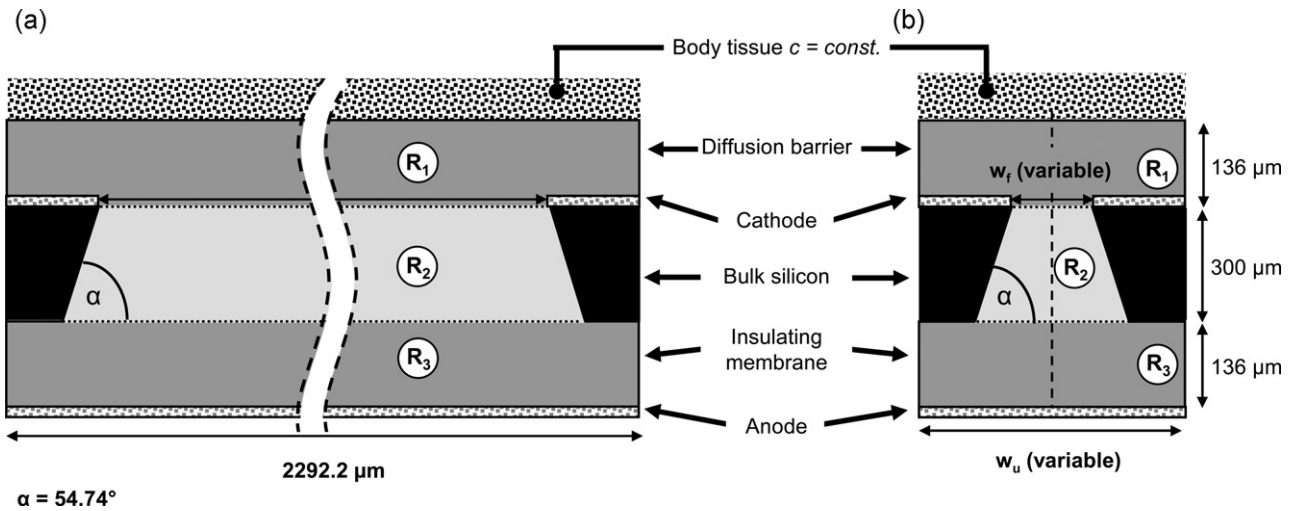
Fig. 2. Dimensions of the unit cell used in simulation of reactant depletion in the glucose fuel cell. (a) Cross-section along the feedhole length. (b) Central cross-section perpendicular to the feedhole length.

ied as summarized in Table 1. In the cathode plane the distance between the feedholes, perpendicular to the feedhole length, was kept constant at 474.2 μm.

2.2. Diffusion coefficients

The diffusion coefficients assigned to the different model regions are summarized in Table 2, and were either determined experimentally or derived from literature data as noted. Based on the effective diffusion coefficient $D_{Glucose}^{eff}$ of glucose through the porous filter membrane (at 37 °C in phosphate buffered saline (PBS), determined experimentally as described in [9]), the effective diffusion coefficient of oxygen $D_{O_2}^{eff}$ through the porous membrane was calculated from the relationship between bulk diffusion coefficient D^0 and the effective diffusion coefficient D^{eff} through a porous membrane:

$$D^{eff} = D^0 \times \chi \tag{3}$$

Herein χ is a geometric factor, accounting for tortuosity, porosity, and constrictivity of the porous media [13]. Assuming that χ is independent of the diffusing species, the effective diffusion coefficient $D_{O_2}^{eff}$ of oxygen in the porous filter membrane can be calculated using the relation.

$$D_{O_2}^{eff} = D_{O_2}^0 \frac{D_{Glucose}^{eff}}{D_{Glucose}^0} \tag{4}$$

where $D_{O_2}^0$ and $D_{Glucose}^0$ are the diffusion coefficients of oxygen and glucose in water, respectively.

2.3. Boundary conditions

The glucose concentration at the interface between diffusion barrier and body tissue was kept constant at 3.0×10^{-3} mol L^{-1} (expected value in tissue [1,16]). Simulations were performed at oxygen concentrations of 6.0×10^{-5} mol L^{-1} ($\cong$7.0% oxygen

saturation) and 3.0×10^{-5} mol L^{-1} ($\cong$3.5% oxygen saturation), corresponding to the typical physiological range of oxygen in tissue [6]. At side walls and feedhole surfaces zero flux conditions were applied.

The maximum reactant flux sustainable by a given feedhole geometry was obtained by setting the reactant concentration at the respective electrode to zero, corresponding to complete consumption of the available species. In addition, concentration profiles were calculated by defining the electrodes as reactant sinks with constant flux density. Here it was assumed that the local reactant flux density at the electrodes is not dependent on reactant concentration. Regarding that the glucose oxidation performance of platinum electrodes is not significantly influenced by glucose concentrations in the range from 0.05×10^{-3} to 50×10^{-3} mol L^{-1} [17] this simplification is reasonable.

In any case the reactant flux densities j_a at the anode and j_c at the cathode were linked to the fuel cell current density i_{Fc} according to

$$\text{Anode:} \quad i_{FC} = j_a z F = j_a 2F \tag{5}$$

$$\text{Cathode:} \quad i_{FC} = j_c z F \frac{(A_{Anode} - A_{Feedhole})}{A_{Anode}}$$
$$= j_c 4F \frac{(A_{Anode} - A_{Feedhole})}{A_{Anode}} \tag{6}$$

Corresponding to Eqs. (1) and (2), the number of transferred electrons z per molecule were assumed to be two for the oxidation of glucose to gluconic acid at the anode [2], and four for the reduction of oxygen to water at a platinum cathode in stagnant solution [18]. F is the Faraday constant, A_{Anode} is the geometrical area of the anode, and $A_{Feedhole}$ corresponds to the cross-sectional area of the feedholes in the cathode plane.

Table 1
Varied feedhole width and corresponding unit cell width used in CFD simulations.

Parameter	Symbol			Range (μm)		
Feedhole widths	w_f	10	50	100	200	500
Corresponding unit cell widths	w_u	484.2	524.2	574.2	674.2	974.2

Table 2
Diffusion coefficients assigned to the model regions depicted in Fig. 2.

Model region	Diffusion coefficient (10^{-10} m^2 s^{-1})	Remarks
R1 and R3: diffusion barrier and insulating membrane	$D_{O_2}^{\text{eff}} = 9.6$	Derived according to Eq. (4)
	$D_{\text{Glucose}}^{\text{eff}} = 2.8 \pm 0.1$	At 37 °C in PBS [9]
R2: free volume of the feedhole	$D_{O_2}^{0} = 30$	At 37 °C in PBS [14]
	$D_{\text{Glucose}}^{0} = 8.5$	At 35 °C in water containing 8×10^{-4} mol L^{-1} NaOH [15]

2.4. Simulation results: influence of feedhole width on maximum fuel cell current density

Fig. 3 shows the simulated influence of feedhole widths on the maximum fuel cell current density. This fuel cell current is either limited by the availability of oxygen at the cathode or glucose at the anode, as indicated.

The results indicate that feedhole width has a contrary effect on the availability of oxygen at the cathode and glucose at the anode. Considering 7.0% oxygen saturation as the upper limit of the physiological range, an optimum is thus found for a feedhole width of 50 μm. Here the availability of both reactants is in equilibrium, the corresponding fuel cell current density amounting to approximately 16 μA cm^{-2}. This value is virtually equal to the maximum possible fuel cell current density, limited by oxygen flux through the diffusion barrier situated in front of the cathode (calculated using Fick's first law of diffusion [19] in combination with Eq. (6) and $D_{O_2}^{\text{eff}}$ from Table 2). Oxygen availability can thus not be significantly improved by a further decrease in feedholes width.

For feedhole widths of less than 200 μm, oxygen availability at the cathode is distinctly less sensitive to increasing feedhole width than the availability of glucose at the anode. Increasing the feedhole width to 200 μm thus gives the opportunity to improve glucose supply to the anode with only little influence on the cathode. Compared to 50 μm wide feedholes, the oxygen-limited fuel cell current density will be only marginally decreased from approximately 16 to 15 μA cm^{-2}. At the same time, the minimum glucose concentration at the anode loaded with 15 μA cm^{-2} will be dramatically increased from virtually zero (complete consumption of the available species) at 50 μm feedhole width, to as much as 0.8×10^{-3} mol L^{-1} with a 200 μm wide feedhole. The corresponding glucose concentration profiles for both feedhole widths are illustrated in Fig. 4. From these also the relatively homogenous distribution of glucose at the anode due to the tapered feedhole geometry is evident. For 200 μm wide feedholes the concentration varies only from a minimum value of 0.8×10^{-3} mol L^{-1} glucose in the corners of the anode plane to a maximum of 1.2×10^{-3} mol L^{-1} glucose in the center of area. For the smaller 50 μm wide feedhole this maximum glucose concentration amounts to only 0.04×10^{-3} mol L^{-1}.

Summarizing, the simulation results suggest that in terms of reactant supply a feedhole width of 50 μm is adequate to supply glucose to the anode up to the oxygen-limited fuel cell current density of 16 μA cm^{-2}. In this case the geometric cathode area will be only reduced by 8% due to the feedholes. For comparison purposes the design with 200 μm wide feedholes is an attractive candidate. Here the wider feedholes promise significantly higher glucose concentration at the anode. However, the increasing feedhole width will result in a by 24% reduced geometrical cathode area. Compared to the cathode with 50 μm wide feedholes, the local current density at this cathode will thus be increased by 21%, which can be expected to result in more pronounced cathode polarization. The fuel cell performance of both designs will be characterized in the following experimental part of this work.

3. Experimental

For fuel cell performance characterization the Raney-platinum cathodes [9], deposited onto silicon substrates with 50 or 200 μm wide tapered feedholes (see Section 2.2), were assembled together with Raney-platinum film anodes [8]. Included into the experimental setup was the diffusion barrier placed in front of the cathode to account for the tissue capsule formation upon implantation. In the following section the individual materials and experimental procedures for fabrication and characterization of the fuel cells are described.

3.1. Cathode preparation

To micro-machine tapered feedholes into 305.5 μm thin silicon wafers (orientation: ⟨1 0 0⟩, double-side polished, n+, P-doped, Okmetic, Vantaa, Finland) standard photolithography in combination with anisotropic potassium hydroxide (KOH) etching [11,12] was used (see supplementary material for schematic depiction of the process).

The deposition of the catalytically active Raney-platinum cathode layer is described in the following; numbers in parentheses correspond to the fabrication steps shown schematically in Fig. 5. At first, the silicon wafer with the micro-machined array of feedholes was attached to a handling wafer using spin-coated photoresist (AZ9260, Microchemicals GmbH, Ulm, Germany) as adhesive. To form a cathode with catalytic activity for oxygen reduction, 20 nm titanium as adhesion interlayer, followed by 500 nm platinum and 500 nm aluminum were consecutively deposited onto the silicon substrate by vapor deposition (1). The top aluminum layer was then protected (2) with a thin layer of photoresist (AZ1518, Microchemicals GmbH, Ulm, Germany), and the wafer was diced into individual chips of 20 by 20 mm. Subsequently, the protective
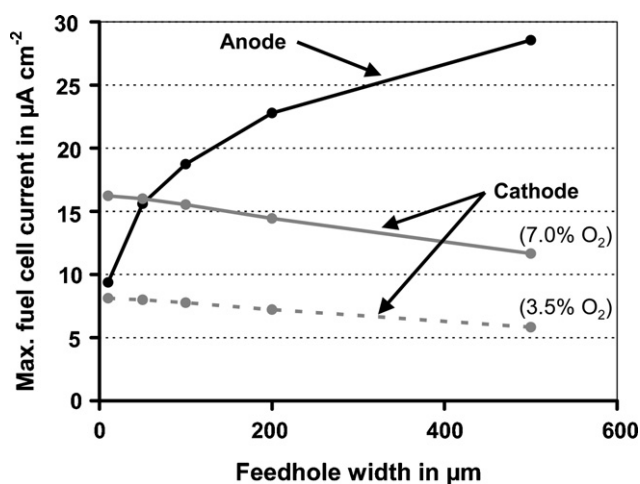

Fig. 3. Influence of feedhole width on the maximum reactant flux at the electrodes (as indicated in the figure) sustainable by a given feedhole geometry, expressed as maximum fuel cell current density according to Eqs. (5) and (6).
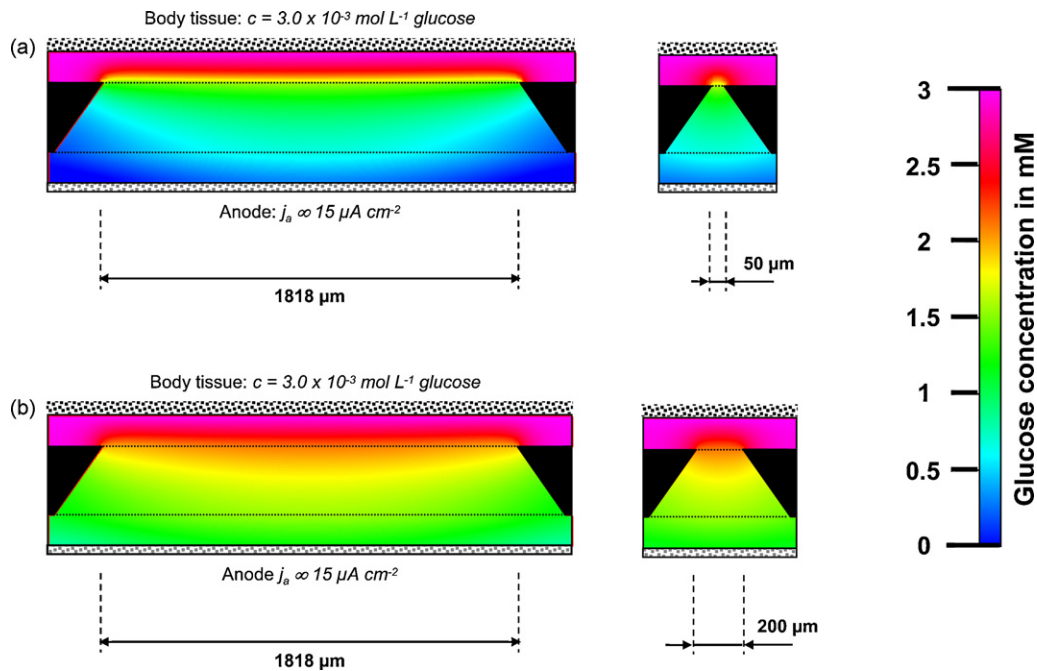
Fig. 4. Steady-state glucose concentration profiles at a current density of $15\,\mu A\,cm^{-2}$. (a) $50\,\mu m$ wide feedhole. (b) $200\,\mu m$ wide feedhole. Shown are cross-sections in the center of the unit cell, both along the feedhole's width (w_f = 50 and $200\,\mu m$) and length (l_f = $1818\,\mu m$).

photoresist as well as the handling wafer was removed from the individual chips using acetone, 2-propanol, and de-mineralized water (3).

To ensure that the catalytically active layer is only formed on the part of the cathode substrate exposed to the testing solution, an approximately 17 by 17 mm patch in the center of the diced chips was protected with conductive carbon cement (Leit-C, Plano, Wetzlar, Germany). Subsequently the unprotected aluminum layer at the edges was selectively removed in $1\,mol\,L^{-1}$ NaOH (4). Following this, the protective layer of conductive carbon cement was removed in isopropanol in an ultra sonic bath. The samples were then annealed for 1 h at $300\,^\circ$C to form a platinum–aluminum alloy (5). Un-alloyed aluminum was afterwards removed in $1\,mol\,L^{-1}$ NaOH, leaving behind the porosified platinum electrode (6). Fur-

ther cleaning was achieved by cyclic voltammetry in $0.5\,mol\,L^{-1}$ H_2SO_4 (20 cycles at $50\,mV\,s^{-1}$ between 1.3 and 0.3 V versus SCE). Calculated from the hydrogen desorption charge, the samples with $200\,\mu m$ wide feedholes showed a by $(13\pm7)\%$ reduced real surface area compared to the electrodes with $50\,\mu m$ wide feedholes. This is close to the theoretically expected 17% reduction due to the wider feedholes.

3.2. Anode fabrication

Raney-platinum film anodes were prepared following the procedure reported elsewhere by the authors [8]. In short, an approximately 30-μm thick zinc layer was electro-deposited onto one side of a 50-μm thick platinum foil (Chempur GmbH,
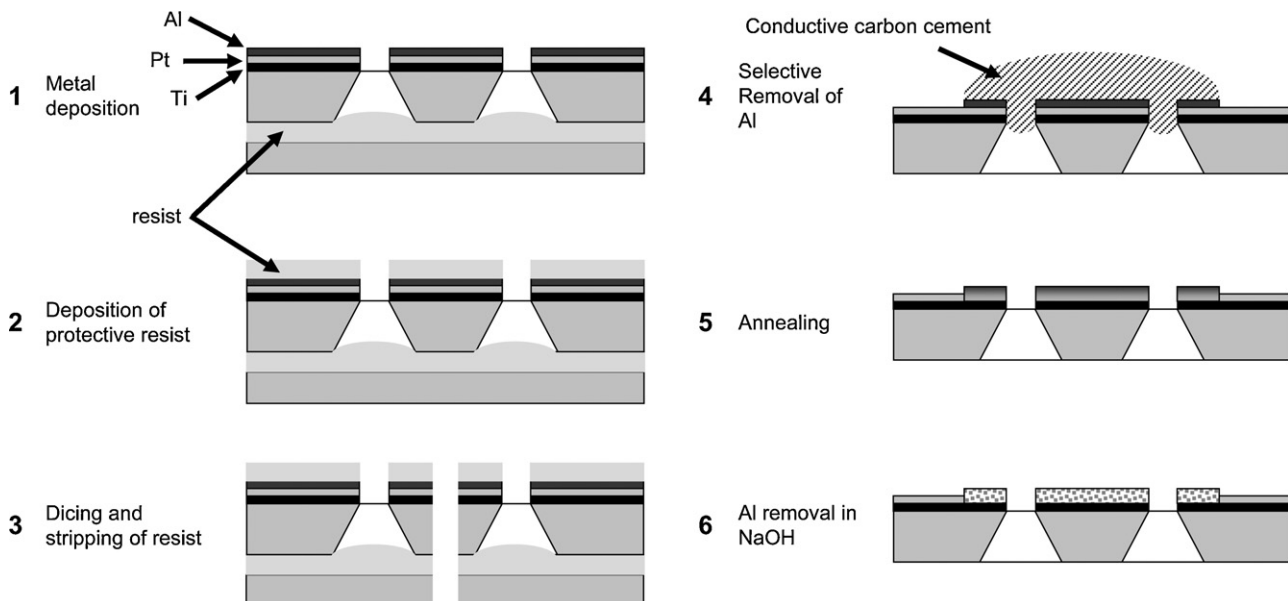

Fig. 5. Schematic of cathode fabrication on top of a silicon substrate with tapered feedholes. See text for explanations.
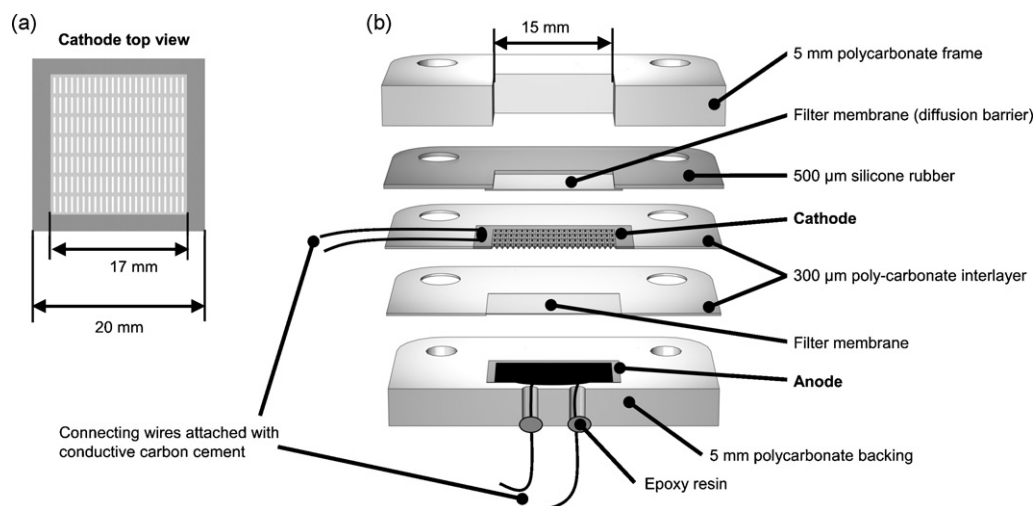
Fig. 6. Fuel cell construction details. (a) Top view of the permeable cathode. The light-colored area represents the slit-array onto which the catalyst is deposited. (b) To-scale cross-sectional view of the binder-less glucose fuel cell assembly. See text for explanations.

Karlsruhe, Germany) and subsequently annealed for 48 h at 200 °C in air atmosphere. After alloy formation, the remaining zinc was removed in 0.5 mol L^{-1} H$_2$SO$_4$, leaving an approximately 30-µm thick porous platinum structure supported on bulk platinum foil. Further cleaning was achieved by cyclic voltammetry sweeps (10 cycles at 10 mV s^{-1}, between 1.3 and 0.3 V versus SCE in de-aerated 0.5 mol L^{-1} H$_2$SO$_4$).

3.3. Fuel cell assembly

In Fig. 6, the to-scale cross-sectional view of the complete fuel cell assembly is shown. To reduce mechanical stress upon assembly, each electrode was placed in the center of a 300-µm thick polycarbonate interlayer frame. For electrical insulation a 136 µm thick porous membrane (Supor-450, Pall, East Hills, New York, USA) is situated between anode and cathode. The same membrane was placed on top of the cathode as diffusion barrier. Together with a 200-µm thick silicone rubber foil on top the whole assembly was clamped between 5 mm polycarbonate fixtures. The influence of contact resistances was eliminated from the measurement by using separate platinum wires for voltage and current, attached to each electrode with conductive carbon cement (Leit-C, Plano, Wetzlar, Germany).

3.4. Performance characterization procedure

For the characterization of fuel cell performance the aseptic reaction chamber and electrical testing system as described in [20] were employed.

To prevent the growth of micro-organisms performance characterization was carried out under sterile conditions at 37 °C. Thereto the fuel cells were autoclaved for 15 min at 121 °C in phosphate buffered saline (PBS tabs, Invitrogen, Karlsruhe, Germany). For electrochemical cleaning the cathodes were then operated for 60 min at an *oxidative* current density of 44.44 µA cm^{-2} at 7.0% oxygen saturation. After the glucose concentration had been adjusted to 3.0 × 10^{-3} mol L^{-1}, the anodes were subject to 5 cyclic voltammetry cycles (at 10 mV s^{-1} between 1.3 and −0.9 V versus SCE, the final cycle ended at −0.5 V) under nitrogen atmosphere (0.0% oxygen saturation). Subsequently the testing solution was replaced through sterile filters with fresh phosphate buffered saline containing 3.0 × 10^{-3} mol L^{-1} glucose (from α-D(+)-glucose monohydrate, Carl Roth, Karlsruhe, Germany).

Both, glucose concentration and range of oxygen saturation were chosen to correspond to the estimated physiological range in body tissue [6,16,21,22]. Thereto the oxygen concentration was adjusted to either 3.5 or 7.0% oxygen saturation by mixing corresponding amounts of air and nitrogen with variable area
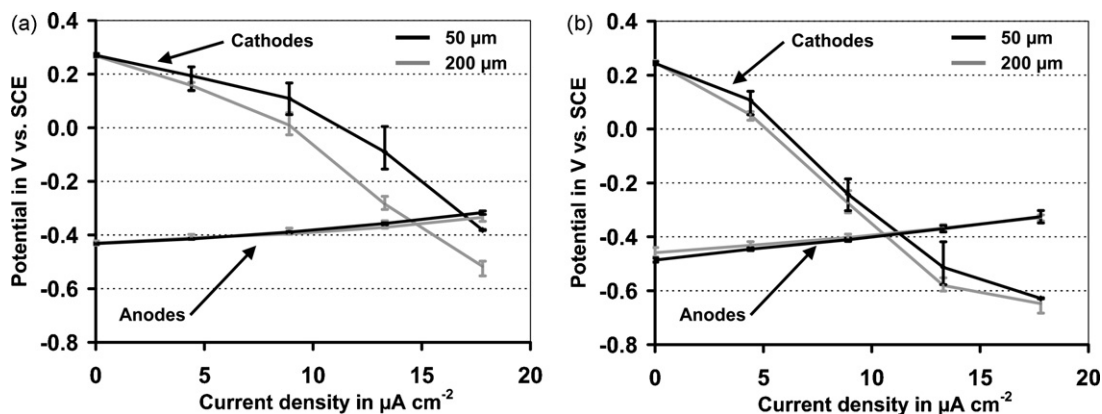

Fig. 7. Individual polarization curves of anode and cathode of operating fuel cells with 50 and 200 µm wide feedholes (as indicated). Recorded at (a) 7.0% oxygen saturation and (b) 3.5% oxygen saturation in the testing solution. Average of triplicate experiments, bars represents maximum and minimum values.

Fig. 8. Polarization curves of complete fuel cells with 50 and 200 μm wide feedholes (as indicated). Recorded at (a) 7.0% oxygen saturation and (b) 3.5% oxygen saturation in the testing solution. Average of triplicate experiments, bars represents maximum and minimum values.
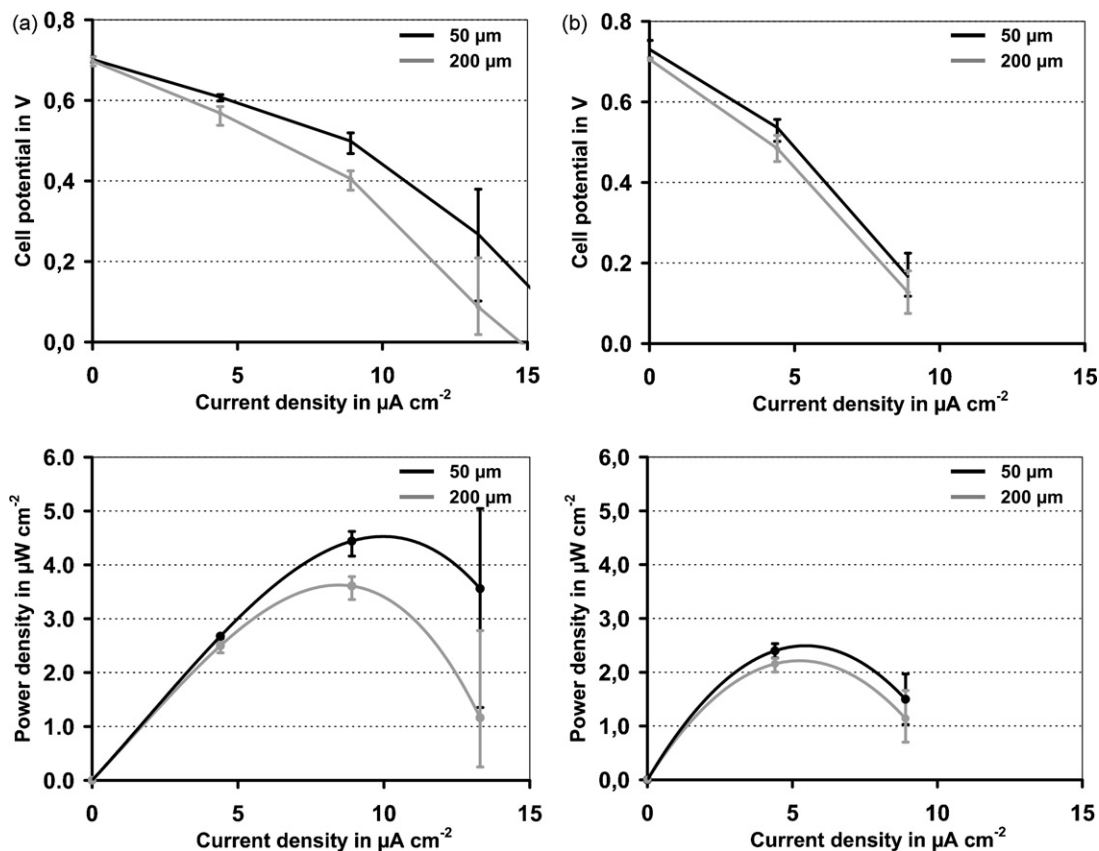
flowmeters (Tubes 112-02TA, Analyt-MTC, Müllheim, Germany; estimated accuracy: ±0.2 percentage points in terms of oxygen saturation; total flow: 2 L min^{-1}). The glucose concentration amounted to 3.0×10^{-3} mol L^{-1} in all experiments.

Since the anode in abiotically catalyzed glucose fuel cells is prone to aging [6,8], always freshly prepared anodes have been used for load experiments at different oxygen concentrations. To obtain stable performance values the load current density was increased in steps of 4.4 μA cm^{-2} every 12 h, starting from open circuit (0.0 μA cm^{-2}) to a maximum of 17.6 μA cm^{-2}.

3.5. Data analysis and presentation

Current density–potential plots were constructed from the stable electrode potentials, recorded versus the saturated calomel reference electrode (SCE; KE11, Sensortechnik, Meinsberg, Germany) after 12 h of operation at a given load current density. The experimental results for power density and potential are reported as (mean value ± sample standard deviation), whereas bars in graphs represent the minimum and maximum value of three experiments conducted in parallel.

In terms of comparison to state-of-the-art the previously published data of our hydrogel-bound activated carbon fuel cells was consulted [6]. However, here the differences in experimental conditions and procedures have to be considered. Especially the higher glucose concentration of 5.0×10^{-3} mol L^{-1} and the lack of a diffusion barrier in front of the fuel cell can be expected to result in higher performance in the previous work [6], as compared to the more realistic experimental conditions of the present work.

4. Results and discussion

4.1. Anode performance

In Fig. 7, the individual polarization curves of cathode and anode during fuel cell operation at 3.5 and also 7.0% oxygen saturation in the testing solution are shown.

With no significant dependence on feedhole size, the anodes exhibit an open circuit potential of − (470 ± 20) mV at 3.5% oxygen saturation. At the higher oxygen saturation of 7.0% it is shifted to by approximately 50 mV more positive values (430 ± 6) mV due to mixed potential formation with oxygen. This potential is by approximately 170 mV (3.5% O$_2$) and 150 mV (7.0% O$_2$) more negative compared to anodes fabricated from carbon-deposited Pt–Bi alloy, although the latter were operated at the higher glucose concentration of 5.0×10^{-3} mol L^{-1} (comparison based on the oxygen sensitivity and the initial open circuit potential reported in [6]). Remarkably, the anode potentials at 3.5% oxygen saturation recorded in this work are more negative than the potential of nominally identical electrodes in oxygen-free solution [8]. We attribute this surprising difference to inter-batch variations in the fabrication process of the electrodes and the slightly different experimental setup in the present work (filter membrane and perforated cathode placed in front of the electrode). Furthermore, separate experiments reported elsewhere [23] revealed that the comparably negative open circuit potential of the Raney-type Pt–Zn anodes is independent of the oxygen-consuming cathode placed in front, and can thus be attributed to improved oxygen tolerance.

Also under load current densities of up to of up to 17.6 μA cm^{-2} the feedhole width in the cathode substrate has no significant influence on anode performance within the investigated range, despite the significant difference in glucose concentration as pre-

dicted by the simulation. This indicates that under the investigated fuel cell operation conditions glucose oxidation is not governed by mass transport, but rather kinetically limited. A corresponding behavior of platinum electrodes has been reported by Wolfson et al. [17], who found no significant influence of varying glucose concentrations in the range of 0.05×10^{-3}–50×10^{-3} mol L^{-1} on performance.

Furthermore, the anodes show no indication of increased polarization due to insufficient glucose supply even beyond the simulated depletion point of $16 \mu A \times cm^{-2}$ for $50 \mu m$ wide feedholes. Besides uncertainties (e.g. the accuracy of literature-derived diffusion coefficients) in the diffusion model, this discrepancy between experiment and simulation can in particular be attributed to the fact that gluconic acid as the main reaction product of glucose oxidation can itself be further oxidized (although at a lower rate) [7,24,25] and thus contribute to the generation of electric current at the anode.

4.2. Cathode performance

Similar to the anodes, the cathodes exhibit an open circuit potential independent of feedhole width. It amounts to $(245 \pm 6) \times mV$ at 3.5% oxygen saturation and increases to (269 ± 4) mV at 7.0% O$_2$. Compared to activated carbon-based cathodes these values are approximately 94 (3.5% O$_2$) and 118 mV (7% O$_2$) more positive, which can be directly attributed to the higher oxygen reduction activity of the platinum catalyst (comparison based on the oxygen sensitivity and the initial open circuit potential reported in [6]).

In contrast to the anodes, the cathodes show a distinctive increase in polarization at higher current densities. Dependent on oxygen saturation, the current density above which this occurs amounts to $4.4 \mu A cm^{-2}$ at 3.5% O$_2$ and $8.8 \mu A cm^{-2}$ at 7.0% O$_2$. This clearly shows the increasing dominance of mass-transport limitation, which is also in agreement with the simulation results (see Section 2.2), predicting that at 3.5% oxygen saturation a maximum fuel cell current density of approximately $8 \mu A cm^{-2}$ can be sustained. In Fig. 7 B, this is apparent as inflection of the polarization curves between the data points at 8.8 and $13.3 \mu A cm^{-2}$, marking the onset of a different electrode reaction (e.g. adsorption and subsequent evolution of hydrogen) once the galvanostatic load current density can no longer be sustained by oxygen-reduction alone [26].

In terms of polarization at 3.5% oxygen saturation, there is no significant difference between the two investigated feedholes widths (50 and 200 μm), despite the 21% higher local current density with $200 \mu m$ wide feedholes due to reduced geometrical cathode area (see also Section 2.4). However, at 7.0% oxygen saturation the influence of the higher local current density becomes evident. Under these conditions cathodes with $200 \mu m$ wide feedholes tend to exhibit more polarization at higher current densities. The absence of this effect at the lower oxygen saturation of 3.5% can be explained by the dominance of oxygen transport on the electrode reaction.

4.3. Performance of the complete fuel cells

In Fig. 8, the dependency of cell voltage and power density on current density is shown for the complete fuel cells. Since feedhole width within the investigated range has no significant influence on the open circuit potentials of anode and cathode (see Sections 4.1 and 4.2), also the overall open circuit potential of the fuel cell is unaffected. Furthermore, the sensitivities of anode and cathode open circuit potential to varying oxygen saturation compensate each other to a large degree. Consequently the differ-

ence in average open circuit voltage is insignificant, amounting to (716 ± 21) and (698 ± 10) mV at 3.5 and 7.0% oxygen saturation, respectively. Compared to our carbon-based fuel cells these values are by approximately 264 and 267 mV higher, respectively.

Also in terms of peak performance at 3.5% oxygen saturation the fuel cells with 50 and $200 \mu m$ wide feedholes do not differ significantly, power densities amounting to (2.4 ± 0.2) and $(2.2 \pm 0.1) \mu W cm^{-2}$, respectively. A different behavior is encountered at 7.0% oxygen saturation, where the slightly better performance of cathodes with $50 \mu m$ wide feedholes also results in an increased peak power density of $(4.4 \pm 0.2) \mu W cm^{-2}$, as compared to the significantly lower $(3.6 \pm 0.3) \mu W cm^{-2}$ reached with $200 \mu m$ wide feedholes. However, despite the diffusion barrier in front of the cathode as well as lower concentrations of glucose and oxygen the performance of both fuel cell designs exceeds the $(3.3 \pm 0.2) \mu W cm^{-2}$ reached with our carbon-based prototypes ([6], operated at 5.0×10^{-3} mol L^{-1} glucose and 21% oxygen saturation).

5. Conclusion

We successfully implemented a novel type of abiotically catalyzed glucose fuel cell that completely obviates the need for polymeric hydrogel binders in electrode fabrication. Compared to earlier approaches with hydrogel-bound particle electrodes the presented concept is endowed with a number of advantages.

Firstly, the high chemical stability of the all-platinum electrodes (as demonstrated by treatment in sulfuric acid as integral part of the fabrication process) effectively mitigates the risk of electrode degradation by hydrolysis and oxidative attack upon prolonged operation. Secondly, the film-type electrodes exhibit inherent electrical conductivity and thus the use of additional current collectors embedded within the electrodes is omitted. This leads to facilitated fabrication and allows for the construction of fuel cells with a by more than 50% reduced overall thickness of $490 \mu m$.

Furthermore, the abdication of hydrogel binders facilitates tailoring the catalytic properties of the electrodes, for instance by the application of thin polymer layers as demonstrated in our earlier works on single electrodes [8,9]. The novel concept is thus a versatile platform for the future development of abiotically catalyzed glucose fuel cells.

Also in terms of performance the novel Raney-platinum fuel cells are advantageous. Despite the inclusion of a diffusion barrier accounting for the expected tissue encapsulation upon implantation they exhibit a maximum power density of up to $(4.4 \pm 0.2) \mu W cm^{-2}$ at 7.0% oxygen saturation, and thus exceed the performance of our previously reported carbon-based fuel cells [6]. Here the higher catalytic activity of platinum cathodes and in particular the increased oxygen tolerance of platinum–zinc anodes [23] result in a relatively high cell voltage of approximately 500 mV. This will also be advantageous in terms of the in practice inevitable DC–DC conversion of the fuel cell voltage to the levels typically required by implant electronics [27].

At current densities beyond the simulated glucose depletion point a decrease in cathode feedhole width from 200 to $50 \mu m$ had no significant effect on anode performance. It can thus be concluded that the application of smaller feedholes is feasible. The consequent increase in geometrical cathode area will reduce cathode polarization and lead to an overall increase in fuel cell performance.

However, as predicted by the simulation and shown experimentally, overall fuel cell performance under physiological conditions is governed by oxygen availability at the cathode. With operation in a mass-transfer limited regime thus only moderate performance enhancement can be anticipated from cathodes with enhanced catalytic activity for oxygen reduction. Under these circumstances

also the additional diffusion resistance to be expected from tissue capsule formation around the implanted fuel cannot be neglected. Future work will therefore not only have to focus on the optimization of long-term stability and biocompatibility in a physiological environment, but also consider possibilities to favorably influence the formation of tissue capsules around implanted foreign bodies.

Acknowledgements

Appendix A. Supplementary data

Supplementary data associated with this article can be found, in the online version, at doi:10.1016/j.jpowsour.2010.08.019.

References

[1] S. Kerzenmacher, J. Ducrée, R. Zengerle, F. von Stetten, J. Power Sources 182 (2008) 1–17.
[2] S. Ernst, J. Heitbaum, C.H. Hamann, Ber. Bunsen-Ges. Phys. Chem. Chem. Phys. 84 (1980) 50–55.
[3] J.R. Rao, G. Richter, F. von Sturm, E. Weidlich, M. Wenzel, Biomed. Eng. 9 (1974) 98–103.
[4] S. Kerzenmacher, R. Sumbharaju, J. Ducrée, R. Zengerle, F. von Stetten, Transducers '07 – Digest of Technical Papers, Lyon, France, 2007, pp. 125–128.
[5] J.R. Rao, G.J. Richter, F. von Sturm, E. Weidlich, Bioelectrochem. Bioenerg. 3 (1976) 139–150.
[6] S. Kerzenmacher, J. Ducrée, R. Zengerle, F. von Stetten, J. Power Sources 182 (2008) 66–75.
[7] U. Gebhardt, J.R. Rao, G.J. Richter, J. Appl. Electrochem. 6 (1976) 127–134.
[8] S. Kerzenmacher, M. Schroeder, R. Brämer, R. Zengerle, F. von Stetten, J. Power Sources 195 (2010) 6516–6523.
[9] S. Kerzenmacher, U. Kräling, M. Schroeder, R. Brämer, R. Zengerle, F. von Stetten, J. Power Sources 195 (2010) 6524–6531.
[10] A.A. Sharkawy, B. Klitzman, G.A. Truskey, W.M. Reichert, J. Biomed. Mater. Res. 37 (1997) 401–412.
[11] G.T.A. Kovacs, N.I. Maluf, K.E. Petersen, Proc. IEEE 86 (1998) 1536–1551.
[12] K.E. Bean, IEEE Trans. Electron Devices 25 (1978) 1185–1193.
[13] J. van Brakel, P.M. Heertjes, Int. J. Heat Mass Transfer 17 (1974) 1093–1103.
[14] J. Jordan, W.E. Bauer, J. Am. Chem. Soc. 81 (1959) 3915–3919.
[15] J.K. Gladden, M. Dole, J. Am. Chem. Soc. 75 (1953) 3900–3904.
[16] D.G. Maggs, R. Jacob, F. Rife, R. Lange, P. Leone, M.J. During, W.V. Tamborlane, R.S. Sherwin, J. Clin. Invest. 96 (1995) 370–377.
[17] S.K. Wolfson, S.L. Gofberg, P. Prusiner, L. Nanis, Trans. Am. Soc. Artif. Int. Organs 14 (1968) 198–203.
[18] D. Pletcher, S. Sotiropoulos, J. Electroanal. Chem. 356 (1993) 109–119.
[19] A. Fick, Ann. Phys. Chem. 170 (1855) 59–86.
[20] S. Kerzenmacher, K. Mutschler, U. Kräling, H. Baumer, J. Ducrée, R. Zengerle, F. von Stetten, J. Appl. Electrochem. 39 (2009) 1477–1485.
[21] N. Chang, W.H. Goodson, F. Gottrup, T.K. Hunt, Ann. Surg. 197 (1983) 470–478.
[22] F. Goda, J.A. Ohara, K.J. Liu, E.S. Rhodes, J.F. Dunn, H.M. Swartz, Oxygen Transport Tissue Xviii 411 (1997) 543–549.
[23] A. Kloke, B. Biller, U. Kräling, R. Zengerle, F. von Stetten, Proceedings of the Eurosensors XXII Conference 2008, Dresden, Germany, 2008, pp. 1416–1419.
[24] S.J. Yao, A.J. Appleby, A. Geisel, H.R. Cash, S.K. Wolfson Jr., Nature 224 (1969) 921–922.
[25] P. Malachesky, G. Holleck, F. McGovern, R. Devarakonda, Proceedings of the 7th Intersociety Energy Conversion Engineering Conference, 1972, pp. 727–732.
[26] C.H. Hamann, W. Vielstich, Elektrochemie, Wiley-VCH, Weinheim, 1998.
[27] S. Kerzenmacher, S. Zehnle, T. Volk, D. Jansen, F. von Stetten, R. Zengerle, Proceedings of PowerMEMS 2008, Sendai, Japan, 2008, pp. 189–192.